

**1 Size-differentiated Export in different Dynamical
2 Regimes in the Ocean**

3 M. Dever¹, D. Nicholson¹, M. Omand², and A. Mahadevan¹

4 ¹Woods Hole Oceanographic Institution, Woods Hole, MA 02543, USA

5 ²Graduate School of Oceanography, University of Rhode Island, Narragansett, Rhode Island, USA

6 Abstract

7 Export of particulate organic carbon (POC) is mainly driven by gravitational sinking.
8 Thus, traditionally, it is thought that larger, faster-sinking particles make up most of the
9 POC export flux. However, this need not be the case in a dynamic oceanic flow field,
10 where the ocean velocity can influence the descent rate of particles. Particles with dif-
11 ferent settling speeds are released in two process-oriented model simulations of an up-
12 per ocean eddying flow to evaluate the impact of (1) the particle number size-spectrum
13 slope, and (2) the ocean dynamics on the respective contribution of the different sinking-
14 velocity classes to POC export. The analysis reveals that the leading export mechanism
15 changes from gravitationally-driven to advectively-driven as submesoscale dynamics be-
16 come more important. The vertical velocity associated with submesoscale dynamics en-
17 hances the contribution of slower-sinking particles in POC export. A steeper particle size
18 spectrum, also increases the contribution of smaller, slower-sinking particles. Implement-
19 ing a remineralization scheme generally decreases the total amount of biomass exported,
20 but its impact is weaker in dynamical regimes where submesoscale dynamics are present
21 and export is advectively-driven. Under specific conditions, remineralization processes
22 counter-intuitively enhance the role of slower-sinking particles to the point where these
23 slower-sinking velocity classes dominate the export, therefore challenging the traditional
24 paradigm for POC export. This study demonstrates that slow-sinking particles are sig-
25 nificant contribution, and at times, can even dominate, the export flux.

26 1 Introduction

27 A major pathway transferring carbon from the atmosphere to the ocean is through
28 photosynthesis and the production of Particulate Organic Carbon (POC) in the upper
29 ocean. Sinking POC then allows the transfer of organic carbon from the upper ocean to
30 the interior, leading to carbon sequestration over long time scales (Falkowski, Barber,
31 & Smetacek, 1998). Understanding the mechanisms driving the export of POC from the
32 ocean's surface to the interior is therefore crucial to better constrain Earth's carbon bud-
33 get.

34 Traditionally, POC export is thought to be mainly driven by larger, faster-sinking
35 particles. This reasoning relies on the concept of competing timescales between reminer-
36 alization and the time required to sink below the base of the mixed layer. The physical
37 processes involved in defining the sinking rate are traditionally assumed to be dominated

38 by gravitational sinking. This is a reasonable assumption if one considers that vertical
39 advective velocities in the ocean are generally much weaker than velocities associated
40 with gravitational sinking.

41 Recent work demonstrates that the presence of mesoscale eddies can enhance car-
42 bon export through two main processes: First, by increasing primary productivity through
43 the injection of nutrients into the euphotic layer, therefore increasing the particle con-
44 centration, logically leading to a greater export (Lévy, Mémery, & Madec, 1998). Sec-
45 ond, by generating larger vertical velocities along the front located at the eddy perime-
46 ter (van Haren, Millot, & Taupier-Letage, 2006; Waite et al., 2016). These studies demon-
47 strate that ocean dynamics potentially play an important role in driving the carbon ex-
48 port from the euphotic layer to the ocean interior. This conclusion is further supported
49 by a recent, yet large, body of literature focusing on ocean dynamics at submeso-scales
50 (1-10 km) and the impact on biogeochemical processes (see reviews in Klein & Lapeyre,
51 2009; Mahadevan, 2016; Thomas, Tandon, & Mahadevan, 2013). Submesoscale dynam-
52 ics are characterized by Rossby numbers of order 1, indicating that relative vorticity as-
53 sociated with ocean currents exceed the planetary vorticity. These regions typically de-
54 velop in filaments in areas where sharp density fronts exist (McWilliams, 2016). In this
55 dynamical regime, geostrophic balance fails and a secondary ageostrophic circulation de-
56 velops across the front, capable of generating large vertical velocities on the order of 100
57 m/day (Fox-Kemper, Ferrari, & Hallberg, 2008; Mahadevan, 2016). On the denser side
58 of the front, the vorticity is cyclonic and associated with downwelling velocities, while
59 anticyclonic vorticity and upwelling is expected on the lighter side of the front. The dis-
60 tribution of relative vorticity across a front is asymmetric and skewed toward cyclonic
61 vorticity (Rudnick, 2001). This asymmetry leads to more localized and more intense down-
62 welling regions, as opposed to weaker and larger upwelling regions (Mahadevan & Tan-
63 don, 2006). Just like at meso-scales, enhanced vertical velocities can generate either a
64 local bloom by supplying nutrients to the sunlit layer of the ocean (Mahadevan, D'Asaro,
65 Lee, & Perry, 2012), or can significantly increase the export of POC to the ocean inter-
66 rior (Estapa et al., 2015; Lévy, Ferrari, Franks, Martin, & Rivière, 2012; Omand et al.,
67 2015).

68 The downwelling velocities $\mathcal{O}(100 \text{ m/day})$ generated at submeso-scales therefore
69 provide a physical mechanism capable of exporting particles over a larger portion of the
70 particle size spectrum. Through this mechanism, smaller particles can efficiently be ex-

ported over timescales shorter than their remineralization timescales, despite their slower sinking velocities. Considering the fact that, although containing less biomass, smaller particles are far more numerous than larger particles, the impact of submesoscale dynamics on the export of POC is potentially significant. Submesoscale processes are, by definition, associated with spatial scales $\mathcal{O}(1 \text{ km})$ and time scales $\mathcal{O}(1 \text{ day})$, which makes it difficult to observe. Additionally, and despite recent methodological progress (McDonnell & Buesseler, 2010), direct measurements of particles sinking velocities are difficult to obtain, and are more often than not inferred from key parameters such as particle type, size, and density.

In this study, we rely on a submesoscale-resolving non-hydrostatic model coupled with a particle-tracking module to explore the necessary conditions for slow-sinking particles to significantly contribute to carbon export, as a function of (1) the dynamics of the flow field, (2) the slope of the sinking velocity spectrum, and (3) the remineralization timescale. Particles in the model are prescribed with both a constant and time-varying sinking velocity to mimic a remineralizing behavior. Particles are released in two fundamentally different flow fields in terms of dynamics: one simulation is dominated by mesoscale dynamics, characterized by low Rossby numbers and weak vertical advective velocities, while the other is dominated by submesoscale dynamics, with fine-scale frontal structures and local Rossby numbers $\mathcal{O}(1)$. Both simulations and the particle-tracking module are described in Section 2. The impact of particles characteristics and ocean dynamics on the export of POC is quantified in Section 3, and discussed in Section 4. Section 5 summarizes the key conclusions of the study.

2 Methods

2.1 Model setup and domains

This study uses a non-hydrostatic, three-dimensional, numerical model called PSOM. Only a brief summary of its characteristics is provided here, as the model is exhaustively described in Mahadevan, Oliger, and Street (1996a, 1996b). The model domain is set in a channel configuration with periodic boundaries in the west and east, and solid boundaries in the south and north. The domain covers 112 km in the x-direction, 304 km in the y-direction, and 1000 m in the vertical (Figure 1). The horizontal resolution is set to 500 m, while the vertical resolution is represented by a stretched grid with 32 levels

ranging in thickness from 1.25 m near the surface to 70 m at the lowermost level. The model is integrated numerically in time and evolves the temperature, salinity, free-surface height, pressure, and three-dimensional velocity fields from an initial state, subject to momentum and buoyancy fluxes applied through the surface boundary conditions.

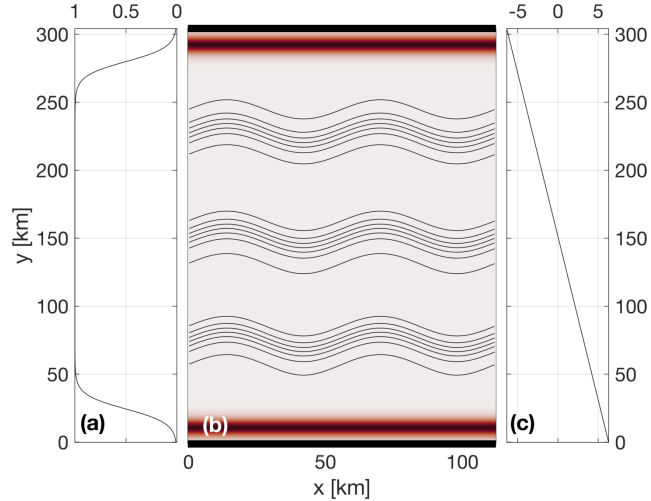


Figure 1. PSOM model setup. (a) Meridional profile of zonal winds scaling coefficient pre-scribed to PSOM, with a tapering at the north and south boundaries to reduce upwelling and downwelling, respectively. (b) Restoration factor used to dampen internal waves reflection at boundaries, as well as curl-driven upwelling and downwelling. (c) Surface net heat flux anomaly superimposed to the heat fluxes prescribed at $y = 150$ km.

The zonal component of the wind stress is prescribed at the surface throughout the model domain ($\tau_y = 0$). Winds stress magnitude is, however, tapered at the northern and southern boundaries to avoid excessive Ekman-driven upwelling and downwelling that could contaminate the middle third of the model domain, where the analysis is focused (Figure 1a). A restoration time scale is prescribed to contain the curl-driven upwelling and downwelling regions generated by the tapering of the wind stress (Figure 1b). The restored regions also limit the reflection of internal waves at the solid boundaries back into the domain. Net surface heat fluxes are homogeneously prescribed throughout the domain. A linear meridional heat flux anomaly is superimposed to maintain a north/south gradient in net surface heat fluxes (Figure 1c). The flux anomaly is zero in the center of the domain and has a slope of $1/24 \text{ W/m}^2/\text{km}$, estimated from the North American Regional Reanalysis (NARR) product (Mesinger et al., 2006).

123 Both wind stress and net heat fluxes are allowed to vary in time. Time series are
 124 computed from measurements collected at Station Papa and available through the Pa-
 125 cific Marine Environmental Laboratory¹. Climatologies of daily zonal wind stress and
 126 net heat fluxes are calculated over the period 2007-2016 to produce a year-long time se-
 127 ries. A squared low-pass filter with a cut-off frequency of 8.5 days is applied to both time
 128 series to remove high-frequency variability. In all experiments, the simulation is allowed
 129 to spin-down, that is with no forcing, for the first 5 days. Forcing is then linearly ramped
 130 up between days 5 and 10, to reach realistic values at day 10.

131 Initial background conditions are determined from a three-dimensional gridded field
 132 of temperature and salinity from ARGO floats (Gaillard et al., 2009; Gaillard, Reynaud,
 133 Thierry, Kolodziejczyk, & von Schuckmann, 2016). ARGO data is averaged monthly over
 134 the period 2002-2012 and two different months are used to initialized *Papa_summer* and
 135 *Papa_winter*. The north-south background density gradient is then intensified into three
 136 fronts located at $y = 75$, $y = 150$, and $y = 225$ km (Figure 1). The amplitude of the
 137 density gradient associated with the three fronts are determined from the probability dis-
 138 tribution function (PDF) of the density gradients measured by underwater gliders de-
 139 ployed around Station Papa over the period 2008-2010 (Pelland, Eriksen, & Cronin, 2016).
 140 To reduce model spin-up time, density fronts are perturbed by a sinusoidal wave with
 141 a wavelength $\lambda = 112/n$, where n is the closest integer to the 1st baroclinic deforma-
 142 tion radius ($n = 2$ in this study). Similar PSOM configurations were successfully used
 143 in previous studies (Mahadevan et al., 2012; Omand et al., 2015).

144 Two main experiments are conducted using the same configuration of PSOM, where
 145 only initial conditions and surface forcings are varied: *Papa_summer* aims at generat-
 146 ing ocean dynamics mimicking conditions int the northeast Pacific in the summertime.
 147 Summer ocean dynamics are characterized by a flow generally in geostrophic balance,
 148 with relatively weak density gradients and low Rossby numbers (< 1). *Papa_winter* aims
 149 at capturing wintertime ocean conditions in the region. A different dynamical regime
 150 is expected to dominate during wintertime, with submesoscale dynamics playing a more
 151 important role. Submesoscale dynamics are characterized by sharper density fronts, filament-
 152 like features and high localized Rossby number (> 1) over spatial scales $\mathcal{O}(1 \text{ km})$. Such
 153 dynamics are more likely to be found in the winter time, where mixed layer depth is deeper

¹ <https://www.pmel.noaa.gov/ocs/Papa>

154 and density gradients enhanced (Thompson et al., 2016). The individual characteristics
 155 of each of *Papa-summer* and *Papa-winter* are detailed below.

156 **2.1.1 *Papa-summer Model Experiment***

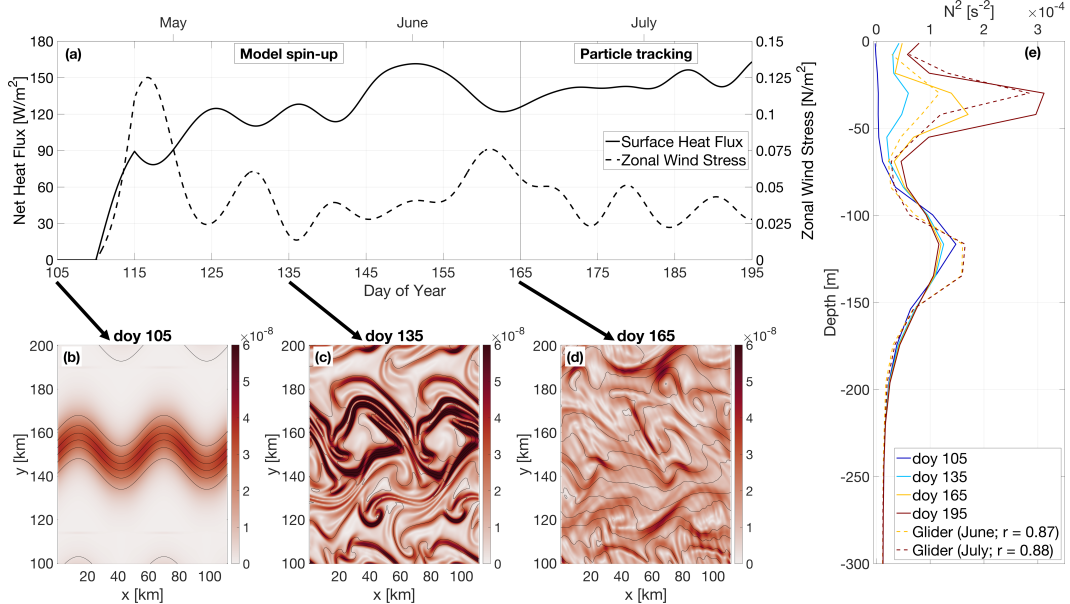
157 In *Papa-summer*, PSOM is initialized based on climatological ARGO data in April.
 158 The magnitude of the density gradient across the front (i.e., frontal sharpness) is set to
 159 3.34×10^{-6} kg/m³/m, which corresponds to the 95th percentile of the PDF of density gra-
 160 dients measured in April from glider data collected in the region (Figure 2 and Table 1).
 161 The model is run with a timestep of 216 s and is allowed to spin-up for 60 days, allow-
 162 ing for the summer stratification to develop. The model is then run for 30 additional days,
 163 saving instantaneous model fields every 3 hours for particle tracking. The month of April
 164 is chosen for initialization so the experiment would capture the onset of positive net heat
 165 fluxes, and the summer restratification that ensues (Figure 2). In this region, the sum-
 166 mer restratification is associated with large primary productivity and therefore large par-
 167 ticle production and potentially export (e.g., fecal pallets, dead phytoplankton; Plant
 168 et al., 2016).

169 **Table 1.** Summary of the key characteristics of PSOM experiments *Papa-summer* and
 170 *Papa-winter*.

	<i>Papa-summer</i>	<i>Papa-winter</i>
Period	April – July	January – March
Spin-up	60 days	50 days
Advection timestep	216 s	108 s
Horizontal diffusivity	1 m ² /s	0.2 m ² /s
Restoration timescale	3 days	15 days
Maximum M ² ($\times 10^{-8}$)	3.20 s ⁻²	33.9 s ⁻²

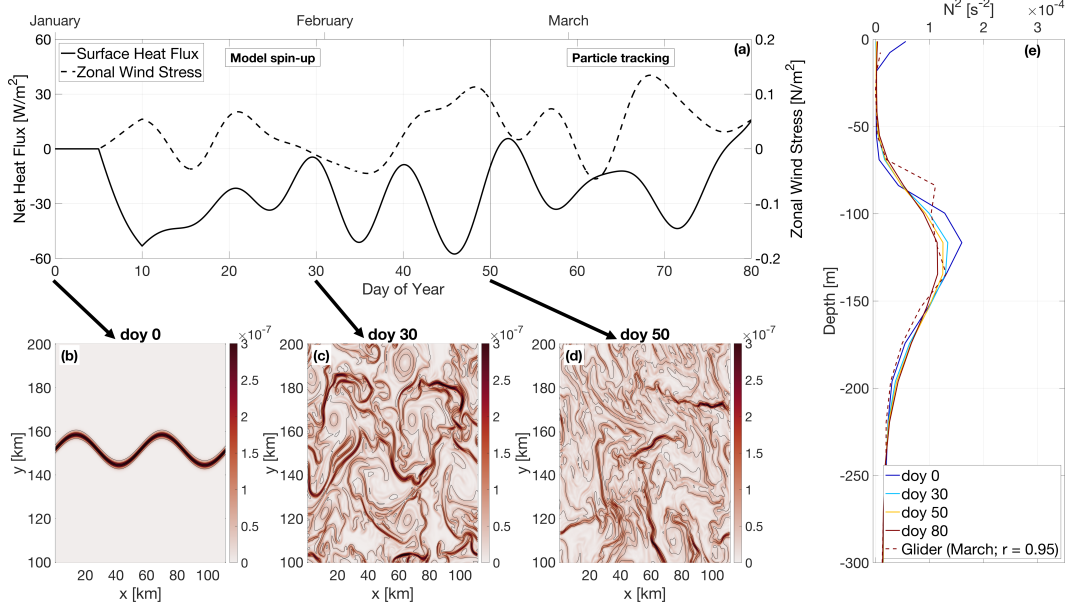
180 **2.1.2 *Papa-winter Model Experiment***

181 In *Papa-winter*, PSOM is initialized based on climatological ARGO data in Jan-
 182 uary. The frontal sharpness is set to 3.54×10^{-5} kg/m³/m, which corresponds to the 99th
 183 percentile of the PDF of density gradients measured in January from glider data collected



171 **Figure 2.** PSOM configuration for *Papa_summer*. (a) Time series of net heat fluxes and
 172 wind stress prescribed at the surface. Notice the positive heat fluxes, as well as downfront winds
 173 (i.e. eastward) persisting throughout the experiment. (b)-(d) horizontal buoyancy gradients
 174 $M^2 = |\nabla_H b|^2$ (in s^{-2}) at day of year (doy) 105, 135, and 165. Black contours show isopycnals (in
 175 kg/m³; CI = 0.01 kg/m³). (e) Vertical profile of the buoyancy frequency N^2 at doy 105, 135, 165,
 176 and 195, showing the development of summer stratification centered at $z = 30$ m (solid lines).
 177 Monthly-average vertical stratification obtained from glider profiles collected in June and July
 178 are superimposed (dashed lines), along with the correlation coefficient between observations and
 179 model outputs.

184 in the region (Figure 3 and Table 1). The model is allowed to spin-up for 50 days allowing
 185 for the prescribed fronts to become unstable. To accommodate the larger density gradients,
 186 the advective timestep is shortened to 108 s, and the horizontal diffusivity is lowered
 187 to 0.2 m²/s. The model is run for 30 additional days, saving instantaneous model
 188 fields every 1.5 hours for particle tracking. The month of January is chosen for initialization
 189 so the experiment would capture the time of year where the mixed layer is the deepest, and Rossby number of O(1) are more likely to occur. The objective is for this
 190 experiment to contrast *Papa_summer* by capturing the statistics of ocean conditions dominated
 191 by submesoscale dynamics.



193 **Figure 3.** PSOM configuration for *Papa_winter*. (a) time series of net heat fluxes and wind
 194 stress prescribed at the surface. Notice the mostly negative heat fluxes, as well as alternating
 195 zonal wind direction. (b)-(d) horizontal buoyancy gradients $M^2 = |\nabla_H b|^2$ (in s^{-2}) at day of
 196 year (doy) 0, 30, and 50. Black contours show isopycnals (in kg/m^3 ; CI = $0.01 kg/m^3$). (e) Ver-
 197 tical profile of the buoyancy frequency N^2 at doy 0, 30, 50, and 80, showing the persistence of
 198 the halocline between $z = 80$ and $z = 180$ m throughout the experiment (solid lines). Monthly-
 199 average vertical stratification obtained from glider profiles collected in March is superimposed
 200 (dashed line), along with the correlation coefficient between observations and model outputs.

201 2.1.3 Validation

202 To ensure that PSOM simulations yielded realistic conditions for both *Papa_summer*
 203 and *Papa_winter*, distributions of horizontal (M^2) and vertical (N^2) buoyancy gradients
 204 are compared with glider observations collected over the period 2008-2009 (Pelland et
 205 al., 2016).

206 During this period, underwater gliders sampled in a “bow-tie” pattern centered on
 207 Station Papa. Gliders sample the water column following a triangular wave, whose shape
 208 is easily affected by currents, due to the slow moving speed of the glider (~ 1 km/hr).
 209 It is therefore challenging to associate a specific spatial scale with gradients computed
 210 between glider profiles, as profile separation distances can be highly variable through depth
 211 and time. To circumvent this issue, horizontal buoyancy gradients are computed between

212 each pair of glider profiles available within one branch of the bow-tie. Each along-track
 213 buoyancy gradient is then associated with a separation scale and a timestamp.

214 Glider-based density gradients are highly affected by internal waves. To filter the
 215 impact of internal waves on the PDF of horizontal buoyancy gradients, only gradients
 216 computed at a scale of ± 1 km of twice the Rossby radius are considered. Rossby radii
 217 are ~ 8 km in winter and ~ 20 km in summer.

218 2.2 Particle Tracking Experiments

219 2.2.1 Particle Advective Scheme

220 To quantify the impact of submesoscale dynamics on the export of Particulate Or-
 221 ganic Matter (POC), Lagrangian particle tracking is used in conjunction with the flow
 222 field obtained from the two experiments described above. Particles are tracked using the
 223 non-divergent velocity field at each face of a grid cell. The velocity field is then linearly
 224 interpolated onto the particle's position. For example, the eastward velocity (x-axis) of
 225 a particle is given by:

$$u(x) = u_{i-1} + \frac{(x - x_{i-1})}{(x_i - x_{i-1})}(u_i - u_{i-1}) \quad (1)$$

226 where the subscripts $i - 1$ and i denote the western and eastern walls of the grid cell
 227 where the particle is located, respectively. This can be re-written as:

$$\frac{\partial x}{\partial t} + \beta x + \delta = 0 \quad (2)$$

228 where $\beta = (u_i - u_{i-1})/\Delta x$ and $\delta = -u_{i-1} - \beta x_{i-1}$ (Döös, Kjellsson, & Jönsson, 2013).

229 This differential equation can be solved analytically for $\beta \neq 0$:

$$x_{t_1} = \left(x_0 + \frac{\delta}{\beta} \right) \exp^{-\beta(t_1 - t_0)} - \frac{\delta}{\beta} \quad (3)$$

230 The time it will take for the particle to reach the eastern or western face of the grid cell
 231 can be computed by taking $x_{t_1} = x_i$ or $x_{t_1} = x_{i-1}$, respectively, and solving for t_1 .
 232 For each advective timestep, the times required for the particle to reach any of the 6 walls
 233 of the grid cell are computed using Equation 3. If any of those times is shorter than the
 234 advective timestep, the particle is advected until it reaches the cell wall. Then the flow

field in the adjacent grid cell is considered and the particle is advected over the remaining time. For each particle tracking experiment, four different classes of particles were released. Each particle class is characterized by a different sinking velocity: 0.025, 0.05, 1, and 5 m/day. The slowest-sinking class was essentially selected to represent non-sinking particles: based on the setup of our experiments, the slowest-sinking particles would take 800 days on average to be exported through gravitational sinking, a timescale much greater than commonly observed remineralization timescales. The fastest-sinking velocity is chosen as a low end-member representing velocity classes that will be exported in its entirety over the course of our experiment. The results presented for the 5 m/day sinking class can therefore be extrapolated to any class with a higher sinking velocity.

In the horizontal, particles are seeded once every 250 m over the entire domain in the x-direction, and for $100 < y < 200$ km in the y-direction. The seeding is centered on the position of the middle front (see Figure 2) and is therefore not affected by artificial features developing at the solid north and south boundaries. In the vertical, eleven of those sheets of particles are seeded every 1 m between 75 and 85 m. This depth range is chosen as it corresponds to the average euphotic depth at Station Papa, defined as the 1% light level. The euphotic depth was computed for the months of February and June over the period 2007-2016 from profiles of Photosynthetically Available Radiation (PAR) collected at Station Papa as part of the long-term monitoring of Line P executed by the Department of Fisheries and Ocean Canada². The average euphotic depth computed for both of these months is around 80 m, which agrees with previously established estimates of the euphotic depth (Harrison, Whitney, Tsuda, Saito, & Tadokoro, 2004; Sherry, Boyd, Sugimoto, & Harrison, 1999).

The particle advective timestep is set to 1.5 hours. The flow field is linearly interpolated in time between model outputs, justifying the higher temporal resolution used for particle tracking in *Papa_winter*. Particle positions are saved every 3 hours, along with key model variables interpolated onto the particle positions (e.g., density, vorticity). Particles are tracked for three weeks (28 days). Each particle-tracking experiment contains 1,971,717 particles per sinking-velocity class, for a total of 9,858,585 particles. Particles located deeper than the maximum winter mixed layer (Pelland et al., 2016; Plant et al.,

² <https://www.waterproperties.ca/linep/index.php>

265 2016, i.e., 100 m;) are considered exported, as they will likely not be re-suspended into
 266 the mixed layer.

267 ***2.2.2 Density and Biomass Spectra***

268 The slope of the size spectrum of particles is traditionally described by the slope
 269 of the log-log curve, ξ , between particle number N and particle radius r (also known as
 270 the Junge slope; White et al., 2015):

$$N(r) = N_0 \left(\frac{r}{r_0} \right)^{-\xi} \quad (4)$$

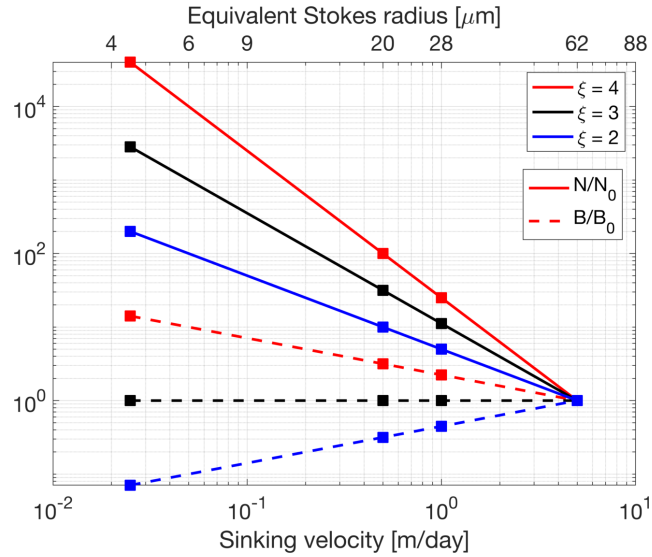
271 where N_0 and r_0 represent a reference particle number and radius, and are chosen ar-
 272 bitrarily. For small particles ($< 400\mu\text{m}$) and relatively cold temperature ($< 15^\circ\text{C}$), it
 273 has been shown that the relationship between particle radius r and sinking velocity w_s
 274 tend to follow Stokes law, with $w_s \propto r^2$ (Bach et al., 2012). Bach et al. (2012) also demon-
 275 strates that Stokes law is generally a lower-bound limit to estimate sinking velocities for
 276 a specific particle size. Assuming a Stokes-like relationship, Equation 4 can thus be re-
 277 written in terms of sinking velocities:

$$N(w_s) = N_0 \left(\frac{w_s}{w_{s_0}} \right)^{-\xi/2} \quad (5)$$

278 For a specific slope and sinking-velocity class, an equivalent number of particles per sim-
 279 ultated particle can thus be computed using Equation 5 (See Figure 4). For example, us-
 280 ing the largest sinking velocity class as a reference (i.e., $w_{s_0} = 5 \text{ m/day}$ and $N_0 = 1,971,717$),
 281 and a spectral slope $\xi = 4$, each simulated particle with a sinking velocity of 0.025 m/day
 282 in fact represent 40,000 particles (Figure 4). The relative biomass of a particle in a spe-
 283 cific sinking-velocity class, $B_p(w_s)$, can be estimated if the biomass is assumed to vary
 284 with the particle's volume. The relative biomass of one particle in a sinking-velocity class
 w_s can therefore be computed using:

$$B_p(w_s) = B_p(w_{s_0}) \left(\frac{w_s}{w_{s_0}} \right)^{3/2} \quad (6)$$

289 where $B_p(w_{s_0})$ is a reference biomass of one particle in the sinking velocity class w_{s_0} . The
 290 total biomass associated with one simulated particle can be obtained by scaling Equa-
 291 tion 6 by the ratio $N(w_s)/N_0$:



286 **Figure 4.** Normalized number of particles (solid) and biomass (dashed)
 287 particle spectrum are shown for three different Junge slope ξ : 4 (red), 0
 288 (black), and 2 (blue).

$$B(w_s) = B_0 \left(\frac{w_s}{w_{s_0}} \right)^{\frac{3-\xi}{2}} \frac{N(w_s)}{N_0} \quad (7)$$

292 where $B_0 = B_p(w_{s_0})$. Combining Equations 5 and 7 yields an expression relating the
 293 biomass associated with a simulated particle for a specific sinking-velocity class and the
 294 spectral slope (Figure 4):

$$B(w_s) = B_0 \left(\frac{w_s}{w_{s_0}} \right)^{\frac{3-\xi}{2}} \quad (8)$$

295 Using the same example as before where $\xi = 4$, if the amount of biomass associated with
 296 one simulated particle in the 5 m/day sinking-velocity class is taken as $B_0 = 1$, then
 297 one simulated particle sinking at 0.025 m/day contains 14.14 units of biomass and a sin-
 298 gle particle contains $14.14/40,000 = 3.5 \times 10^{-4}$ units of biomass (see Figure 4). This
 299 normalized formulation of particle number and biomass (Equations 5 and 8) presents the
 300 advantage that the impact of spectral slope on the relative export of biomass can be quan-
 301 tified without needing a large number of particle-tracking experiments. For the purpose
 302 of this study, only the relative amount of biomass is relevant. For simplicity, we there-
 303 fore define a normalized biomass unit as $B_0 = 1$.

304 **2.2.3 Particle Remineralization Scheme**

305 Remineralization of particles as they sink through the water column evidently im-
 306 pact the export of biomass. Slow-sinking particles therefore are subject to shallower rem-
 307 ineralization than fast-sinking particles. In this study, the impact of remineralization is
 308 considered through the implementation of a time-dependent sinking velocity. Remin-
 309 eralization processes driving remineralization rates are complex, species-dependent, and
 310 generally not well-understood. In the absence of a consensus on a general functional form
 311 of particle remineralization, we rely on an idealized relationship linking carbon content
 312 and time. This implicitly assumes that the biomass content of a particle diminishes in
 313 time proportionally to the particle volume. Remineralization is thus modeled as an ex-
 314 ponential decrease of biomass with time at a rate k (Iversen & Ploug, 2010, 2013):

$$B(t) = B^0 \exp(-kt) \quad (9)$$

315 where B^0 denotes the biomass content at $t = 0$ days, and $k = 0.13 \text{ day}^{-1}$. This rem-
 316 ineralization rate determined by Iversen and Ploug (2010) is independent of particle sink-
 317 ing velocity, and seems to generally agree with other findings, despite the large uncer-
 318 tainties (Iversen & Ploug, 2013; Ploug, Iversen, Koski, & Buitenhuis, 2008). The change
 319 in biomass with time is in turn expected to affect the sinking velocity of the particle. Given
 320 that $B \propto w^{3/2}$ (see Equation 6), a time-varying sinking velocity is imposed to parti-
 321 cles in all sinking-velocity classes using:

$$w_s(t) = w_s^0 \exp\left(-\frac{2kt}{3}\right) \quad (10)$$

322 where w_s^0 is the initial sinking velocity at $t = 0$ days. Particles are classified based on
 323 their initial sinking-velocity. However, it is worth noting that over the length of the particle-
 324 tracking experiments including remineralization (28 days), particles slow down by more
 325 than 90% of their initial velocity.

326 **3 Results**

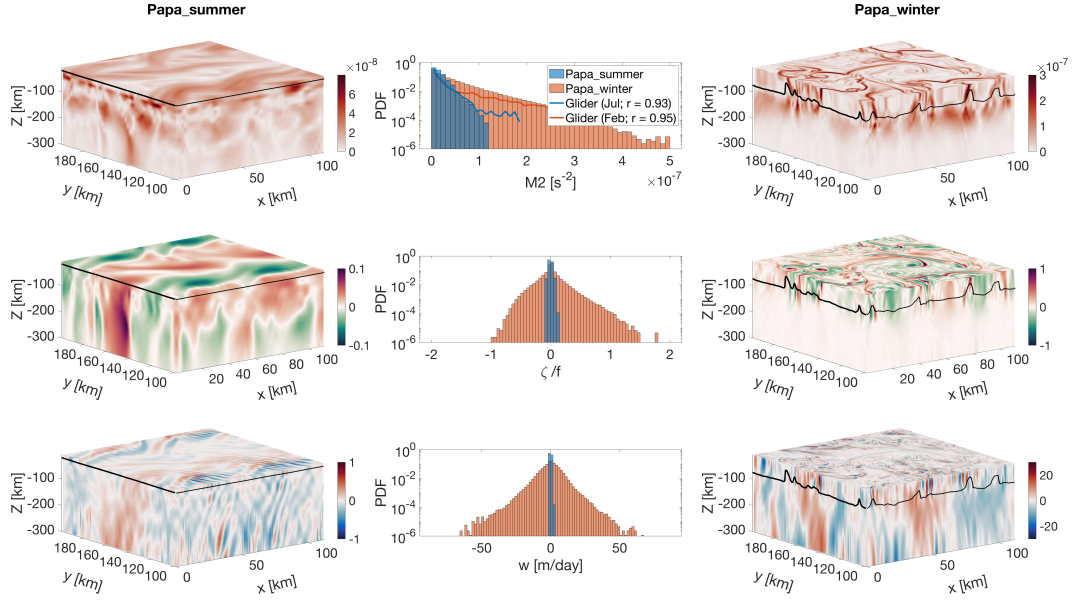
327 **3.1 Physical model**

328 Two model experiments are designed to capture different dynamical conditions ob-
 329 served in the northeast Pacific Ocean in summer and winter. *Papa-summer* is initial-
 330 ized in early spring (doy 105) when the water column is characterized by a relatively deep

mixed layer (~ 100 m) and a halocline present between 100 and 150 m (Figure 2). The forcing by a realistic, positive, net heat flux generates the restratification of the water column, with the development of a strong thermocline between 25 and 50 m leading to the shoaling of the mixed layer and a subsurface peak in N^2 at about 30 m (see Figure 2). A comparison between model outputs and monthly-averaged density profiles from underwater gliders collected in June and July over the period 2008-2009 yields correlation coefficients of $r = 0.87$ and $r = 0.88$, respectively. These correlation coefficients suggest that *Papa-summer* captures reasonably well the vertical spring and summer conditions in the northeast Pacific Ocean.

In the horizontal, the prescribed density fronts progressively become unstable within the first 60 days of the experiment (Figure 2). During this time, the Total Kinetic Energy (TKE) contained in the model domain slowly increases before reaching a maximum at doy 162, where it remains relatively constant for the rest of the simulation. The flattening of the TKE curve is used to determine the time necessary for the simulation to spin-up, hence determining the start day of the particle-tracking experiments. The ocean dynamics associated with *Papa-summer* are characterized using PDFs of horizontal buoyancy gradients ($M^2 = |\nabla_H b|^2$), vertical velocities (w), and Rossby numbers computed from the normalized vertical component of the relative vorticity ($\text{Ro} = (\partial v / \partial x - \partial u / \partial y) / f$; Figure 5).

The largest horizontal buoyancy gradients are observed above the thermocline ($z < 50$ m) and along the halocline (100-200 m), and range between 0 and $1.2 \times 10^{-7} \text{ s}^{-2}$ (Figure 5). These relatively weak density gradients result in low Rossby numbers $O(0.1)$, positive on the denser (north) side of the front, and negative on the lighter (south) side of the front. Corresponding vertical velocities are consistently weaker than 1 m/day ($< 10^{-5}$ m/s) and are characterized by regions of weak upwelling and downwelling on the order of 10 km, associated with the meandering of the front (Bower & Rossby, 1989). Alternating bands of upwelling and downwelling at $O(1 \text{ km})$ spatial scale are superimposed, likely caused by propagating internal waves. Coherent vertical velocity structures are homogeneous to depths much greater than the mixed layer depth (~ 25 m; Figure 2). The amplitude of the vertical velocity field coincides with the expected order of magnitude given by the scaling $w \propto RofU/N$ (Mahadevan, 2016): using $\text{Ro} \sim 0.1$ (Figure 5), $N \sim 10^{-2} \text{ 1/s}$ (Figure 2), $f \sim 10^{-5} \text{ 1/s}$, and $U \sim 0.01 \text{ m/s}$, we obtain $w \sim 10^{-6}$



350 **Figure 5.** Snapshots of M^2 (top), ζ/f (middle), and w (bottom) half-way through the par-
 351 ticle tracking experiment for *Papa_summer* (left and blue) and *Papa_winter* (right and red),
 352 with the Mixed Layer Depth indicated by the solid black line. The corresponding Probability
 353 Distribution Functions (PDFs) are shown in the center. Note the changing color scales between
 354 *Papa_summer* and *Papa_winter*. Histograms of M^2 computed from glider data at Station Papa in
 355 February (blue line) and July (red line) are superimposed in the top middle panel.

369 m/s. The agreement between the scaling and the model outputs suggest that PSOM is
 370 capable of reproducing a realistic vertical flow field.

371 *Papa_winter* is, on the other hand, initialized in the winter (doy 0) with the ob-
 372 jective to capture a time period where the mixed layer depth is deeper (~ 100 m) and
 373 density gradients more pronounced (Pelland et al., 2016). At this time of year, the wa-
 374 ter column in this region is characterized by the presence of a deep halocline between
 375 100 and 150 m. After spin-up, the vertical stratification remains consistent throughout
 376 the model run, and compares well to the vertical profile obtained from glider observa-
 377 tions for the month of March ($r = 0.95$; see Figure 3). In the horizontal, prescribed den-
 378 sity fronts are much sharper than in *Papa_summer* ($O(1$ km) vs. $O(10$ km)). Because
 379 of these stronger density gradients, combined with the alternating zonal winds and con-
 380 stantly negative surface heat flux, the fronts become unstable more rapidly than in *Papa_summer*
 381 (Figure 3). As a result, TKE starts to plateau at doy 48. The experiment is considered
 382 spun-up by doy 50 and the particle-tracking experiment is initialized.

383 The frontal structures visible in the horizontal buoyancy gradient field are logically
 384 associated with filaments of relatively high Rossby numbers, regularly exceeding $O(1)$
 385 (Figure 3). The PDF of Rossby numbers reveals a positively-skewed distribution of Rossby
 386 numbers ($s = 0.68$). This is in agreement with the fact the relative vorticity is more
 387 likely to be cyclonic than anticyclonic, based on conservation of potential vorticity (Hoskins
 388 & Bretherton, 1972). Regions with a high Rossby number are localized and located in
 389 the mixed layer exclusively. In places where the local Rossby number reaches $O(1)$, geostrophic
 390 balance is lost and a vertical secondary ageostrophic circulation develops to slump the
 391 isopycnals and return to a more stable geostrophically-driven flow. This ageostrophic sec-
 392 ondary circulation therefore generates “hot spots” of higher vertical velocities. The fine-
 393 scale structures in the vertical velocity field corresponding to Rossby numbers $O(1)$ can
 394 be seen in Figure 3, with local vertical velocities up to 60 m/day ($\sim 7 \times 10^{-4}$ m/s; Fig-
 395 ure 5). Contrarily to the PDF of Rossby numbers, the distribution of vertical velocities
 396 demonstrate a negative skewness ($s = -0.25$). This is in agreement with the theory: In
 397 fact, positive vertical vorticity is associated with the dense side of a density front, where
 398 Rossby numbers are positive and vertical velocities negative (Mahadevan, 2016). Once
 399 again, the amplitude of these vertical velocity hot spots is coherent with the scaling $w \propto$
 400 $Ro f U / N$: using $Ro \sim 1$, $N \sim 10^{-2}$ 1/s, $f \sim 10^{-5}$ 1/s, and $U \sim 0.1$ m/s, we obtain
 401 $w \sim 10^{-4}$ m/s. This demonstrates the capabilities of PSOM to resolve sharp frontal
 402 features at the kilometer scale, as well as the ageostrophic circulation associated with
 403 those fronts.

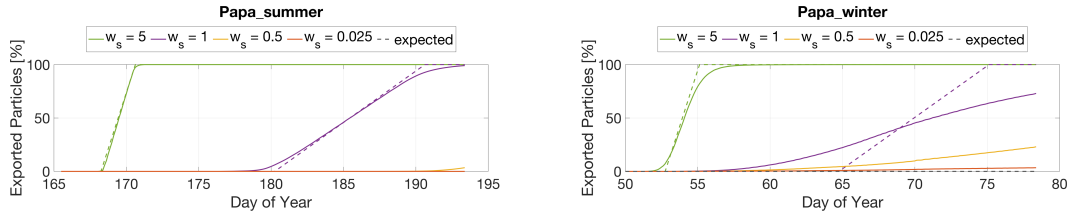
404 Comparing *Papa-summer* and *Papa-winter* highlights the different dynamical regimes
 405 in the two experiments. In *Papa-winter*, density fronts tend to be sharper, meaning larger
 406 density gradients over shorter spatial scales. When computed at the kilometer-scale, the
 407 PDF of horizontal buoyancy gradients in *Papa-winter* exhibits a longer tail than in *Papa-summer*
 408 (Figure 5). When compared to observations, the PDFs of M^2 in *Papa-summer* and *Papa-winter*
 409 demonstrate a correlation with observations of $r = 0.93$ and $r = 0.95$, respectively

410 The wider PDF of vertical velocities in *Papa-winter* shows advective velocities that
 411 match and exceed typical gravitational sinking velocities, particularly for smaller, and
 412 therefore slower-sinking, particulate organic material. The secondary ageostrophic cir-
 413 culation that develops at submeso-scales (i.e., $Ro O(1)$) therefore generates an export
 414 mechanism that directly competes with the traditional paradigm that relies on gravita-
 415 tional sinking leading the export of particulate matter in the ocean.

416 3.2 Particle tracking

417 Both model experiments described above were then used to investigate the rela-
 418 tionship between ocean dynamics and particle export, using Lagrangian particle-tracking.
 419 In this study, particles are considered "exported" once located below the depth of the
 420 winter mixed layer, which roughly corresponds to the 100 m depth horizon at Station
 421 Papa. Choosing the winter mixed layer as the export depth is most appropriate, as it
 422 reduces the chances of particles being re-entrained into the mixed layer the following win-
 423 ter. We first consider the case of conservatives particles that do not remineralize in or-
 424 der to better identify the effects of ocean dynamics and spectral slope on export.

425 The percentage of simulated particles being exported with time is shown in Fig-
 426 ure 6 for both *Papa-summer* and *Papa-winter*. As expected, the faster-sinking particles
 427 are exported earlier and in larger proportions. For *Papa-summer* specifically, only the
 428 two fastest sinking-velocity classes (5 and 1 m/day) are exported within the first 28 days,
 429 while the other sinking-velocity classes do not significantly export particles over this time
 430 period (< 5%). In fact, time series of exported particles closely follow the curves derived
 431 from considering gravitational sinking only (Figure 6).



432 **Figure 6.** Percentage of particles located below 100 m as a function of time in *Papa-summer*
 433 (left), and *Papa-winter* (right). Expected percentages of exported particles based on gravitational
 434 sinking only are indicated with dashed lines.

435 Time series of exported particles in *Papa-winter* present major differences. In ev-
 436 ery sinking-velocity class, particles reach the export depth faster than expected from grav-
 437 itational sinking. This early arrival of particles is accentuated as the sinking-velocity de-
 438 creases, ranging from about 1 day early for particles sinking at 5 m/day, to about 10 days
 439 early for particles sinking at a rate of 1 m/day. Sinking-velocity classes that are not ex-
 440 pected to reach the export depth within the first 28 days now significantly contribute
 441 to export within the first 15 days of the simulation. Over 20% of particles sinking at 0.5

442 m/day is now exported, versus less than 5% in *Papa-summer*. About 5% of particles sink-
 443 ing at 0.025 m/day are exported. However, more time is now necessary to export 100%
 444 of the simulated particles. This can be seen in the gentler slopes of the export curves ob-
 445 served in *Papa-winter* than in *Papa-summer*.

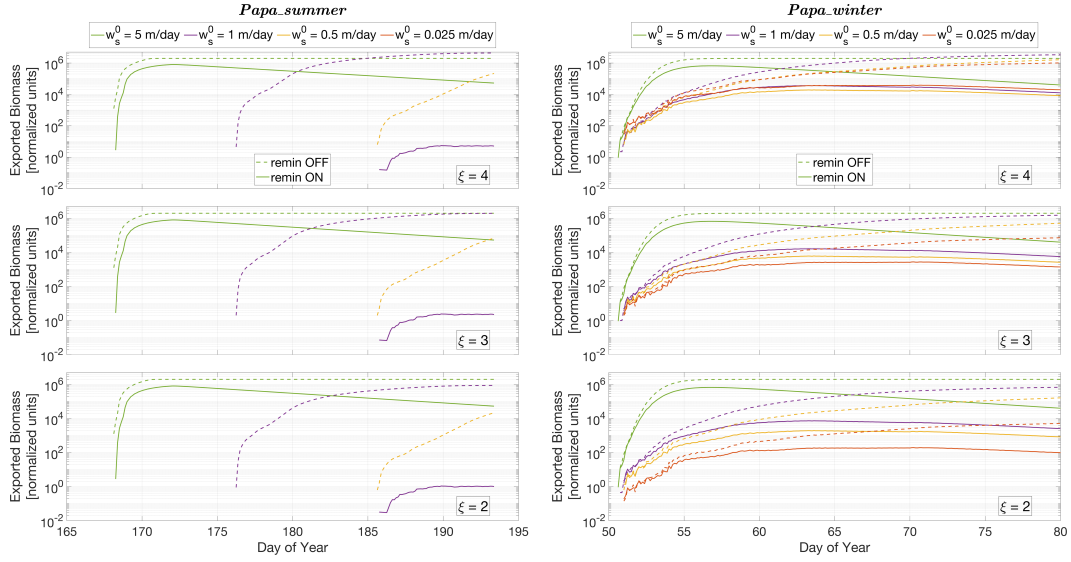
446 Particles released in *Papa-winter* are thus exported faster and in greater number
 447 than expected from gravitational sinking only. Eventually, all sinking particles would be
 448 exported in both *Papa-summer* and *Papa-winter*, if particles were tracked for a long enough
 449 period of time. Particles, and specifically slow-sinking ones, are however expected to rem-
 450 ineralize on timescales shorter than their export timescale. The impacts of remineral-
 451 ization on export are presented and discussed in Sections 3.3 and 4.2.

452 The presence of submesoscale dynamics therefore increases the number of exported
 453 slow-sinking simulated particles, by anywhere between a few percent and tens of percents,
 454 depending on the sinking-velocity class. This has large implications on the amount of
 455 biomass exported, as slower-sinking particles are far more numerous than faster-sinking
 456 particles, despite containing less biomass (Figure 4). While the number of simulated par-
 457 ticles that are exported is only a function of the modeled flow field, the exported biomass
 458 also depends on the Junge slope (see Equation 8).

459 The impact of ocean dynamics on the respective contributions of the different sink-
 460 ing velocity classes to the total exported biomass is fairly intuitive: For a specific Junge
 461 slope, the presence of submesoscale dynamics enhance the role played by slower-sinking
 462 particles in biomass export, and thus decrease the importance of faster-sinking particles
 463 (Figure 7). This is a logical results in sight of the increase in the number of particles ex-
 464 ported when submesoscales features are present (Figure 6). The sinking class dominat-
 465 ing export, however, is highly dependent on the Junge slope parameter. As the Junge
 466 slope parameter increases, the particle spectrum steepens, and the contribution of slower-
 467 sinking particles to the total exported biomass increases, sometimes dominating biomass
 468 export. For example, after 28 days, the 1 m/day exports 50%, 100%, and 125% of the
 469 biomass exported by the 5 m/day class when $\xi = 2, 3$, and 4, respectively.

474 3.3 Particle Remineralization

475 Including remineralization of particles (Equation 9) significantly impacts the rel-
 476 ative importance of sinking and advection to export for each particle class. In *Papa-summer*,



470 **Figure 7.** Amount of biomass exported in normalized units by each sinking velocity class in
 471 *Papa_summer* (left), and *Papa_winter* (right), for three different Junge slopes: $\xi = 4$ (top)
 472 ($\xi = 3$ (middle), and $\xi = 2$ (bottom; see Figure 4). Dashed lines represent the case without remineraliza-
 473 tion, while solid lines include the remineralization scheme described in Section 2.2.3.

477 particle export associated with a specific sinking-velocity class is delayed when reminer-
 478 alization is implemented, because particles slow down as they are remineralized (Equa-
 479 tion 10 and Figure 7). In our simulations, particles sinking at 5 m/day reach the export
 480 horizon about 3 hours later when remineralization is included. The impact of reminer-
 481 alization intensifies as the sinking velocity weakens: particles sinking at 1 m/day reach
 482 the export horizon 9.5 days later when remineralization is considered.

483 The total amount of biomass is also reduced compared to the case with no rem-
 484 ineralization. The difference between the two cases is time dependent, and increases with
 485 the age of the particle, as particles further remineralize. The impact of remineralization
 486 on the amount of biomass exported intensifies as the sinking velocity decreases. In fact,
 487 in *Papa_summer* with no remineralization, several sinking-velocity classes contribute to
 488 the biomass export, with slower-sinking particles contributing significantly less than faster-
 489 sinking particles (dash lines in Figure 7). Once remineralization is implemented, no par-
 490 ticles in the slowest sinking class (0.5 m/day) reach the export horizon and the contri-
 491 bution of the 1 m/day class is reduced by 5-6 orders of magnitude depending on the slope
 492 of the biomass spectra (see Figure 4). Similarly to the case with no remineralization, a

493 change in the Junge slope impacts the contribution of slower-sinking velocity classes. This
 494 can be seen in the amount of biomass exported by the 1 m/day sinking-velocity class:
 495 A negative slope (i.e., $\xi = 4$) leads to a maximum biomass of about 6, while a positive
 496 slope (i.e., $\xi = 2$) leads to a maximum biomass of 1. Both of these amount of exported
 497 biomass represent less than 1% of the total exported biomass, making the contribution
 498 to export from this sinking-velocity class virtually insignificant.

499 In *Papa_winter*, particles of all sinking-velocity classes tend to be exported more
 500 rapidly than in *Papa_summer* due to stronger vertical velocities. The difference in ex-
 501 ported biomass between the cases with and without remineralization is therefore rela-
 502 tively small for the first 5 days of the time series, as particles have not had time to sig-
 503 nificantly remineralize yet but are already behind exported. As particles age, reminer-
 504 alization has an increasing impact and the difference in total exported biomass increases
 505 at a rate controlled by the remineralization rate in Equation 9. Similarly to *Papa_summer*,
 506 the total amount of biomass exported by a specific sinking-velocity class decreases as the
 507 Junge slope decreases (i.e., the sinking-velocity spectra flattens). An interesting result
 508 to be noticed is the fact that, when $\xi = 4$ and remineralization is implemented, the amount
 509 of biomass exported from the 0.025 m/day sinking-velocity class exceeds the amount of
 510 biomass exported by both the 0.5 and 1 m/day sinking-velocity classes. This result only
 511 occurs when a negative slope of the biomass spectrum is combined with remineraliza-
 512 tion.

513 4 Discussion

514 4.1 Physical model

515 *Papa_summer* and *Papa_winter* experiments were designed to statistically capture
 516 the ocean dynamics at Station Papa (145°W , 50°N) in the northeast Pacific Ocean. Af-
 517 ter spin-up, the model demonstrated similar distribution of both horizontal (M^2) and
 518 vertical (N^2) density gradients than observed using underwater gliders (see Figures 2,
 519 3, and 5). The two experiments, however, show significantly different distributions of M^2 ,
 520 where the winter distribution has a longer tail, suggesting sharper density gradients. The
 521 tail of the wintertime distribution is only partially captured by the glider data, due to
 522 the fact that underwater gliders sample gradients at a maximum resolution of about 10

523 km, while the model resolution is 500 m and therefore allows sharp submesoscale fronts
 524 and filaments to be captured in the distribution.

525 Studies investigating submesoscale dynamics traditionally focused on regions where
 526 the presence of submesoscale fronts and filaments are established, such as western bound-
 527 ary currents with strong gradients (D'Asaro, Lee, Rainville, Harcourt, & Thomas, 2011;
 528 Thomas, Taylor, Ferrari, & Joyce, 2013), or at the edge of mesoscale features (van Haren
 529 et al., 2006; Waite et al., 2016). The seasonality in submesoscale dynamics captured in
 530 the glider dataset at Station Papa, and reflected in the model experiments, echoes find-
 531 ings of recent observational studies conducted at a similar latitude in the Atlantic Ocean
 532 demonstrating the intensification of submesoscale dynamics in the wintertime (Buck-
 533 ham et al., 2016; Thompson et al., 2016). Despite being sometimes qualified as an "eddy
 534 desert" with low kinetic energy (Chelton, Schlax, & Samelson, 2011), wintertime ocean
 535 characteristics in the eastern part of the Pacific subpolar gyre suggest the presence of
 536 submesoscale features: strong density gradients, localized Rossby numbers of the order
 537 1 and larger, a balanced Richardson number $Rib = \frac{f^2 N^2}{M^4}$ smaller than 1, a positively
 538 skewed distribution in vorticity, and a negatively skewed distribution of vertical veloc-
 539 ities (see Figure 5; Buckingham et al., 2016; Rudnick, 2001; Thomas, Tandon, & Mahade-
 540 van, 2013).

541 Strong downward velocities are hypothesized to enhance POC export by advect-
 542 ing slower-sinking particles out of the mixed layer. *Papa-winter* indeed exhibits verti-
 543 cal velocities more than 20 times larger than in *Papa-summer*. The vertical currents in
 544 *Papa-winter*, however, tend to be much patchier than the weaker vertical currents ob-
 545 served in *Papa-summer*. Because both particle production and downward vertical ve-
 546 locities present a high degree of patchiness, it requires a certain level of covariance be-
 547 tween the two fields for the export to effectively be enhanced (Mahadevan et al., 2012).
 548 A more realistic seeding strategy for Lagrangian particles, such as one guided by biolog-
 549 ical tracers, would likely provide important information towards a better understand-
 550 ing of the effects of patchiness on POC export at submeso-scales

551 The hypothesis tested in this study is that submesoscale activity enhances export
 552 of particulate matter at Station Papa. The wintertime intensification in submesoscale
 553 activity has the potential to indeed enhance export (see discussion below). However, the
 554 seasonal cycle in submesoscale activity is out of phase with the one in net community

productivity, which peaks in the spring and summertime when the mixed layer is shallower (Plant et al., 2016). Two mechanisms are therefore present to potentially sustain a year-long POC export: In the winter, less particulate material is present in the mixed layer, but active submesoscale dynamics tend to enhance the POC export by advecting the more numerous slower-sinking particles into the ocean interior. In the summer, the production of POC is much larger, but export tends to be dominated by gravitational sinking, which discriminate against slower-sinking particles.

562 4.2 Particle export

563 Analyses of particle tracking experiments reveal that the role played by slow-sinking
564 particles in POC export depends on two main characteristics: (1) the dynamics of the
565 ocean flow field, and (2) the slope of the size spectrum (i.e., the Junge slope coefficient
566 ξ).

567 Mixed layer ocean dynamics at station Papa change significantly between the win-
568 ter and the summer. In the winter, submesoscale dynamics are intensified and sharp fronts
569 and filaments develop in the mixed layer. This change in dynamics has a clear impact
570 on the amount of particles exported for all sinking-velocity classes modeled in this ex-
571 periment. First, particles in all sinking-velocity class generally reach the export depth
572 faster. This is the most significant result, as export from any sinking-velocity class is char-
573 acterized by two competing timescales: its export timescales (i.e., the time it takes for
574 a particle to reach the export depth), and its remineralization timescales. The former
575 evidently needs to be shorter than the latter to efficiently export POC. Second, parti-
576 cles are exported more gradually. While particles in a sinking-velocity class reach the
577 export depth over shorter timescale, it takes longer to export the same number of par-
578 ticles as in the summer. This is due to the upward vertical current, re-suspending ma-
579 terial that would otherwise sink, and thus delaying its export. Keeping in mind the com-
580 peting timescales mentioned above, it leads to interesting questions: Is it more efficient
581 to export more faster-sinking particles—less numerous but containing more biomass—and
582 no slower-sinking particles, like in *Papa_summer*? Or is export greater when less faster-
583 sinking particles are exported, but more slower-sinking particles, much more numerous,
584 also contribute to the export, like in *Papa_winter*?

585 In the absence of remineralization, the net effect of submesoscale dynamics on biomass
 586 export depends on the Junge slope coefficient. Over the course of our simulation, the to-
 587 tal amount of biomass exported is consistently enhanced when $\xi = 4$ (10 to 60% increase)
 588 in the presence of submesoscale dynamics. For a flat biomass spectrum ($\xi = 3$), the ex-
 589 port enhancement due to submesoscale dynamics is always smaller than 20%. When $\xi =$
 590 2, the amount of biomass exported in the presence of submesoscale dynamics varies be-
 591 tween 95 and 110% of the export observed in the summer, when submesoscale dynam-
 592 ics are not active. Therefore, to address the questions formulated above, export is only
 593 enhanced in the presence of submesoscale dynamics if the slope of the size spectrum is
 594 steep enough to compensate for the re-suspension of faster-sinking particles by upwards
 595 vertical currents at submesoscales.

596 Introducing remineralization processes significantly decreases the total amount of
 597 biomass exported. Counter-intuitively, however, remineralization processes further strengthen
 598 the impact of submesoscale dynamics on export. The increase in exported biomass when
 599 comparing summertime and wintertime is larger when remineralization processes are in-
 600 cluded, and also increase with larger ξ . Total exported biomass almost doubles when $\xi =$
 601 4, and increases by 5 and 20% for $\xi = 2$ and $\xi = 3$, respectively. This can be explained
 602 by the fact that remineralization processes have a greater impact on sinking-velocity classes
 603 that rely on gravitational sinking to be exported, as remineralization tends to slow these
 604 particles down and thus prolongs their export timescales. In the summer, almost the en-
 605 tirety of the sinking velocity spectrum is therefore affected as all classes rely on grav-
 606 itational sinking for export. In the winter, however, slower-sinking particles are exported
 607 through advective processes. Their export timescale is little affected by remineralization
 608 processes as it only depends on local ocean dynamics, leading to a greater net export than
 609 when remineralization is not considered.

610 The contribution of a particle class to POC export generally increases with the sinking-
 611 velocity. That is, faster-sinking particles tend to dominate the export signal and the curve
 612 of exported biomass versus sinking-velocity has a positive slope. To have a greater con-
 613 tribution of a slower-sinking velocity class, the following condition must be satisfied:

$$N_{slow} > N_{fast} \times \left(\frac{w_{s_{fast}}}{w_{s_{slow}}} \right)^{\frac{3-\xi}{2}} \quad (11)$$

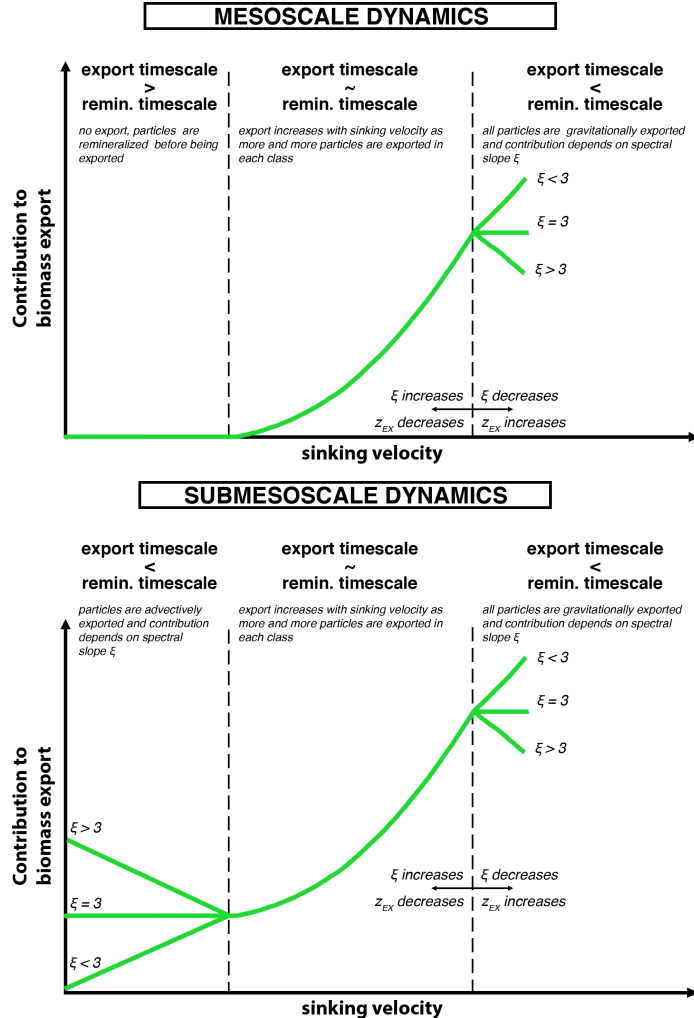
614 where N is the number of simulated particles exported, w_s is the sinking velocity and
 615 ξ is the Junge slope coefficient (see Equation 4).

616 In a gravitationally-driven system (i.e., weak submesoscale activity), this can only
 617 be achieved by having $N_{slow} \sim N_{fast}$ and $\xi > 3$, as there are no mechanism capable
 618 of selectively exporting slower-sinking particles (i.e., $N_{slow} \leq N_{fast}$). Junge slopes greater
 619 than 3 are regularly observed in the ocean (Kostadinov, Siegel, & Maritorena, 2009; White
 620 et al., 2015). Our results suggest that, in these conditions, the export of biomass is dom-
 621 inated by an intermediate sinking-velocity class that sinks fast enough to be 100% ex-
 622 ported ($N_{slow} = N_{fast}$; see Figure 8). Because of the negative slope in the biomass spec-
 623 trum, any particle class sinking at a faster rate will not contribute as much to the biomass
 624 export. The intermediate class responsible for the largest part of the export signal will
 625 vary with time and space as it depends on the parameter ξ , as well as on the export depth.
 626 As ξ increases, the sinking-velocity of the dominant class decreases (see Equation 11).
 627 A deeper export depth would have the opposite effect and increase sinking-velocity of
 628 the dominant class (Figure 8). Implementing remineralization processes only shifts the
 629 curve shown in Figure 8 towards faster-sinking classes: as particle remineralize, a larger
 630 portion of the sinking-velocity spectrum will not contribute to POC export, and a faster
 631 initial sinking-velocity is required for the export timescale to be shorter than the rem-
 632 ineralization timescale.

636 In a system affected by submesoscale dynamics, localized strong downwelling ver-
 637 tical currents are generated. This effectively shortens the export timescale of slower-sinking
 638 particles, entering a regime where export timescales are shorter than remineralization
 639 timescales (Figure 8). In this regime, slower-sinking particles significantly contribute to
 640 POC export. In this study, sinking-velocity classes that did not contribute to POC ex-
 641 port in a mesoscale regime, are found to contribute up to 30% of POC export in the most
 642 extreme case, where $\xi = 4$. Implementing remineralization process has little to no im-
 643 pact on the respective contributions of the different sinking-velocity classes as the im-
 644 pact of remineralization is smaller in advectively-driven export mechanism, as opposed
 645 to gravitationally-driven.

646 5 Conclusion

647 The main conclusions of this study are:



633 **Figure 8.** Schematics showing the respective contribution to export of particles with different
 634 sinking velocities in (top) a gravitationally-driven system (i.e., weak submesoscale dynamics), and
 635 (bottom) an advectively-driven system (i.e., strong submesoscale dynamics).

- 648 1. Submesoscale activity at station Papa is enhanced in the wintertime, leading to
 649 larger vertical velocities than in the summertime. The export mechanism in the
 650 winter is thus driven by advective sinking, as opposed to gravitational sinking in
 651 the summertime.
- 652 2. Submesoscale dynamics generally enhance export by increasing the contribution
 653 of slower-sinking particles to POC export by increasing the number of particle ex-
 654 ported through advective sinking. The contribution of slower-sinking particles in
 655 ageostrophic flows is at least significant, and can be dominant in specific condi-
 656 tions.

657 3. Contribution of slower-sinking particles to POC export depends on the slope of
658 the particle size spectra (i.e., Junge Slope), that controls the relative number of
659 particles per size class. Three cases emerge in this study:

- 660 (a) If the Junge slope is smaller than 3, larger particles contribute most to export
661 independently of flow dynamics, as there are no mechanism capable of selec-
662 tively exporting slower-sinking particles.
- 663 (b) If the Junge slope equals 3, the respective contributions of the different size classes
664 depend on the dynamical characteristics of the flow, as it influences the num-
665 ber of particles being exported. If 100% of the particles is exported in all sink-
666 ing classes, then each class contributes equally to POC export.
- 667 (c) If the Junge slope is greater than 3, ocean dynamics become the determining
668 factor on which classes dominate: in a mostly geostrophic flow with weak ver-
669 tical velocities, an intermediate sinking-velocity class will dominate POC ex-
670 port. In a flow with ageostrophic circulation leading to larger vertical veloci-
671 ties, slower sinking classes can potentially dominate export.

672 4. Remineralization processes reduce the contribution of slower-sinking particles when
673 export dynamics are dominated by gravitational sinking (i.e., in a geostrophic flow).
674 As flow dynamics become ageostrophic, advective sinking leads the export and rem-
675 ineralization processes have a limited impact.

676 Acknowledgments

677 The authors acknowledge support from the National Aeronautics and Space Ad-
678 ministration as part of the EXport Processes in the global Ocean from RemoTe Sens-
679 ing (EXPORTS) program - grant NNX16AR48G. We would like to thank A. Thomp-
680 son (Caltech) for his useful comments and suggestions, N. Pelland (NOAA) and Char-
681 lie Eriksen (University of Washington) for sharing the glider data collected at Ocean Sta-
682 tion Papa, as well as Sebastian Essink for his assistance in developing the particle-tracking
683 code. All data used in this manuscript are publicly available: Ocean Station Papa data
684 is available on PMEL's website (<https://www.pmel.noaa.gov/ocs/Papa>) and gridded
685 ARGO products can be downloaded at <http://www.seanoe.org/data/00348/45945>.
686 Glider data, model outputs, and particle trajectories are freely available on request.

687 **References**

- 688 Bach, L. T., Riebesell, U., Sett, S., Febiri, S., Rzepka, P., & Schulz, K. G. (2012).
 689 An approach for particle sinking velocity measurements in the 3400 μm size
 690 range and considerations on the effect of temperature on sinking rates. *Marine*
 691 *Biology*, 159(8), 1853–1864. doi: 10.1007/s00227-012-1945-2
- 692 Bower, A. S., & Rossby, T. (1989). Evidence of Cross-Frontal Exchange Processes
 693 in the Gulf Stream Based on Isopycnal RAFOS Float Data. *Journal of Phys-*
 694 *ical Oceanography*, 19(9), 1177–1190. doi: 10.1175/1520-0485(1989)019<1177:
 695 EOCFEP>2.0.CO;2
- 696 Buckingham, C. E., Naveira Garabato, A. C., Thompson, A. F., Brannigan, L.,
 697 Lazar, A., Marshall, D. P., … Belcher, S. E. (2016). Seasonality of sub-
 698 mesoscale flows in the ocean surface boundary layer. *Geophysical Research*
 699 *Letters*, 43(5), 2118–2126. doi: 10.1002/2016GL068009
- 700 Chelton, D. B., Schlax, M. G., & Samelson, R. M. (2011). Global observations of
 701 nonlinear mesoscale eddies. *Progress in Oceanography*, 91(2), 167–216. doi: 10
 702 .1016/j.pocean.2011.01.002
- 703 D’Asaro, E., Lee, C., Rainville, L., Harcourt, R., & Thomas, L. (2011). Enhanced
 704 Turbulence and Energy Dissipation at Ocean Fronts. *Science*, 332(6027), 318–
 705 322. doi: 10.1126/science.1201515
- 706 Döös, K., Kjellsson, J., & Jönsson, B. (2013). TRACMASS – A Lagrangian Trajec-
 707 tory Model. In *Preventive methods for coastal protection* (pp. 225–249). Heidel-
 708 berg: Springer International Publishing. doi: 10.1007/978-3-319-00440-2_7
- 709 Estapa, M. L., Siegel, D. A., Buesseler, K. O., Stanley, R. H. R., Lomas, M. W., &
 710 Nelson, N. B. (2015). Decoupling of net community and export production
 711 on submesoscales in the Sargasso Sea. *Global Biogeochemical Cycles*, 29(8),
 712 1266–1282. doi: 10.1002/2014GB004913
- 713 Falkowski, P. G., Barber, R. T., & Smetacek, V. (1998). Biogeochemical Controls
 714 and Feedbacks on Ocean Primary Production. *Science*, 281(5374), 200–206.
 715 doi: 10.1126/science.281.5374.200
- 716 Fox-Kemper, B., Ferrari, R., & Hallberg, R. (2008). Parameterization of Mixed
 717 Layer Eddies. Part I: Theory and Diagnosis. *Journal of Physical Oceanogra-*
 718 *phy*, 38(6), 1145–1165. doi: 10.1175/2007JPO3792.1
- 719 Gaillard, F., Autret, E., Thierry, V., Galaup, P., Coatanoan, C., & Loubrieu, T.

- 720 (2009). Quality Control of Large Argo Datasets. *Journal of Atmospheric*
721 *and Oceanic Technology*, 26(2), 337–351. Retrieved from <https://doi.org/10.1175/2008JTECH0552.1> doi: 10.1175/2008JTECHO552.1
- 722
723 Gaillard, F., Reynaud, T., Thierry, V., Kolodziejczyk, N., & von Schuckmann, K.
724 (2016). In situ-based reanalysis of the global ocean temperature and salinity
725 with isas: Variability of the heat content and steric height. *Journal of Climate*,
726 29(4), 1305–1323. doi: 10.1175/JCLI-D-15-0028.1
- 727 Harrison, P. J., Whitney, F. A., Tsuda, A., Saito, H., & Tadokoro, K. (2004).
728 Nutrient and Plankton Dynamics in the NE and NW Gyres of the Sub-
729 arctic Pacific Ocean. *Journal of Oceanography*, 60(1), 93–117. doi:
730 10.1023/B:JOCE.0000038321.57391.2a
- 731 Hoskins, B. J., & Bretherton, F. P. (1972). Atmospheric Frontogenesis Models:
732 Mathematical Formulation and Solution. *Journal of the Atmospheric Sciences*,
733 29(1), 11–37. doi: 10.1175/1520-0469(1972)029<0011:AFMMFA>2.0.CO;2
- 734 Iversen, M. H., & Ploug, H. (2010). Ballast minerals and the sinking carbon flux in
735 the ocean: carbon-specific respiration rates and sinking velocity of marine snow
736 aggregates. *Biogeosciences*, 7(9), 2613–2624. doi: 10.5194/bg-7-2613-2010
- 737 Iversen, M. H., & Ploug, H. (2013). Temperature effects on carbon-specific respi-
738 ration rate and sinking velocity of diatom aggregates - potential implications
739 for deep ocean export processes. *Biogeosciences*, 10(6), 4073–4085. doi:
740 10.5194/bg-10-4073-2013
- 741 Klein, P., & Lapeyre, G. (2009). The Oceanic Vertical Pump Induced by Mesoscale
742 and Submesoscale Turbulence. *Annual Review of Marine Science*, 1(1), 351–
743 375. doi: 10.1146/annurev.marine.010908.163704
- 744 Kostadinov, T. S., Siegel, D. A., & Maritorena, S. (2009). Retrieval of the particle
745 size distribution from satellite ocean color observations. *Journal of Geophysical*
746 *Research*, 114(C9), C09015. doi: 10.1029/2009JC005303
- 747 Lévy, M., Ferrari, R., Franks, P. J. S., Martin, A. P., & Rivière, P. (2012). Bringing
748 physics to life at the submesoscale. *Geophysical Research Letters*, 39(14), n/a–
749 n/a. doi: 10.1029/2012GL052756
- 750 Lévy, M., Mémery, L., & Madec, G. (1998). The onset of a bloom after deep winter
751 convection in the northwestern Mediterranean sea: mesoscale process study
752 with a primitive equation model. *Journal of Marine Systems*, 16(1-2), 7–21.

- 753 doi: 10.1016/S0924-7963(97)00097-3
- 754 Mahadevan, A. (2016). The Impact of Submesoscale Physics on Primary Produc-
755 tivity of Plankton. *Annual Review of Marine Science*, 8(1), 161–184. doi: 10
756 .1146/annurev-marine-010814-015912
- 757 Mahadevan, A., D'Asaro, E., Lee, C., & Perry, M. J. (2012). Eddy-Driven Strat-
758 ification Initiates North Atlantic Spring Phytoplankton Blooms. *Science*,
759 337(6090), 54–58. doi: 10.1126/science.1218740
- 760 Mahadevan, A., Olinger, J., & Street, R. (1996a). A Nonhydrostatic Mesoscale Ocean
761 Model. Part II: Numerical Implementation. *Journal of Physical Oceanog-
762 raphy*, 26(9), 1881–1900. Retrieved from [http://journals.ametsoc.org/doi/abs/10.1175/1520-0485\(1996\)026%3C1881:ANMOMP%3E2.0.CO;2](http://journals.ametsoc.org/doi/abs/10.1175/1520-0485(1996)026%3C1881:ANMOMP%3E2.0.CO;2)
763 doi:
764 <http://journals.ametsoc.org/doi/abs/10.1175/1520-0485%281996%29026%3C1881%3AANMOMP%3E2.0.CO%3B2> doi:
765 10.1175/1520-0485(1996)026(1881:ANMOMP)2.0.CO;2
- 766 Mahadevan, A., Olinger, J., & Street, R. (1996b). A Nonhydrostatic mesoscale ocean
767 model. Part I: Well-posedness and scaling. *Journal of Physical Oceanography*,
768 26(9), 1868–1880. doi: 10.1175/1520-0485(1996)026(1868:ANMOMP)2.0.CO;
769 2
- 770 Mahadevan, A., & Tandon, A. (2006). An analysis of mechanisms for submesoscale
771 vertical motion at ocean fronts. *Ocean Modelling*, 14(3-4), 241–256. doi: 10
772 .1016/J.OCEMOD.2006.05.006
- 773 McDonnell, A. M. P., & Buesseler, K. O. (2010). Variability in the average sinking
774 velocity of marine particles. *Limnology and Oceanography*, 55(5), 2085–2096.
775 doi: 10.4319/lo.2010.55.5.2085
- 776 McWilliams, J. C. (2016). Submesoscale currents in the ocean. *Proceedings of the
777 Royal Society A: Mathematical, Physical and Engineering Science*, 472(2189).
- 778 Mesinger, F., DiMego, G., Kalnay, E., Mitchell, K., Shafran, P. C., Ebisuzaki, W.,
779 ... Shi, W. (2006). North american regional reanalysis. *Bulletin of the Ameri-
780 can Meteorological Society*, 87(3), 343-360. doi: 10.1175/BAMS-87-3-343
- 781 Omand, M. M., D'Asaro, E. A., Lee, C. M., Perry, M. J., Briggs, N., Cetini, I.,
782 & Mahadevan, A. (2015). Eddy-driven subduction exports particulate or-
783 ganic carbon from the spring bloom. *Science*, 348(6231), 222–225. doi:
784 10.1126/science.1260062
- 785

- Pelland, N. A., Eriksen, C. C., & Cronin, M. F. (2016). Seaglider surveys at Ocean Station Papa: Circulation and watermass properties in a meander of the North Pacific Current. *Journal of Geophysical Research: Oceans*, 121, 6816–6846. doi: 10.1002/2016JC011920
- Plant, J. N., Johnson, K. S., Sakamoto, C. M., Jannasch, H. W., Coletti, L. J., Riser, S. C., & Swift, D. D. (2016). Net community production at Ocean Station Papa observed with nitrate and oxygen sensors on profiling floats. *Global Biogeochemical Cycles*, 30(6), 859–879. doi: 10.1002/2015GB005349
- Ploug, H., Iversen, M. H., Koski, M., & Buitenhuis, E. T. (2008). Production, oxygen respiration rates, and sinking velocity of copepod fecal pellets: Direct measurements of ballasting by opal and calcite. *Limnology and Oceanography*, 53(2), 469–476. doi: 10.4319/lo.2008.53.2.0469
- Rudnick, D. L. (2001). On the skewness of vorticity in the upper ocean. *Geophysical Research Letters*, 28(10), 2045–2048. doi: 10.1029/2000GL012265
- Sherry, N. D., Boyd, P. W., Sugimoto, K., & Harrison, P. J. (1999). Seasonal and spatial patterns of heterotrophic bacterial production, respiration, and biomass in the subarctic NE Pacific. *Deep-Sea Research Part II: Topical Studies in Oceanography*, 46(11-12), 2557–2578. doi: 10.1016/S0967-0645(99)00076-4
- Thomas, L. N., Tandon, A., & Mahadevan, A. (2013). Submesoscale processes and dynamics. In *Ocean modeling in an eddying regime* (p. 17-38). American Geophysical Union (AGU). doi: 10.1029/177GM04
- Thomas, L. N., Taylor, J. R., Ferrari, R., & Joyce, T. M. (2013). Symmetric instability in the Gulf Stream. *Deep Sea Research Part II: Topical Studies in Oceanography*, 91, 96–110. doi: 10.1016/j.dsr2.2013.02.025
- Thompson, A. F., Lazar, A., Buckingham, C., Naveira Garabato, A. C., Damerell, G. M., & Heywood, K. J. (2016). Open-Ocean Submesoscale Motions: A Full Seasonal Cycle of Mixed Layer Instabilities from Gliders. *Journal of Physical Oceanography*, 46(4), 1285–1307. doi: 10.1175/JPO-D-15-0170.1
- van Haren, H., Millot, C., & Taupier-Letage, I. (2006). Fast deep sinking in Mediterranean eddies. *Geophysical Research Letters*, 33(4), L04606. doi: 10.1029/2005GL025367
- Waite, A. M., Stemmann, L., Guidi, L., Calil, P. H. R., Hogg, A. M. C., Feng, M., ... Gorsky, G. (2016). The wineglass effect shapes particle export to the deep

- 819 ocean in mesoscale eddies. *Geophysical Research Letters*, 43(18), 9791–9800.
- 820 doi: 10.1002/2015GL066463
- 821 White, A. E., Letelier, R. M., Whitmire, A. L., Barone, B., Bidigare, R. R., Church,
- 822 M. J., & Karl, D. M. (2015). Phenology of particle size distributions
- 823 and primary productivity in the North Pacific subtropical gyre (Station
- 824 ALOHA). *Journal of Geophysical Research: Oceans*, 120(11), 7381–7399.
- 825 doi: 10.1002/2015JC010897